

Article

Bonding Characteristics and Chemical Inertness of Zr–Si–N Coatings with a High Si Content in Glass Molding

Li-Chun Chang ^{1,2}, Yu-Zhe Zheng ³, Yung-I Chen ^{3,*}, Shan-Chun Chang ³ and Bo-Wei Liu ³

¹ Department of Materials Engineering, Ming Chi University of Technology, New Taipei City 24301, Taiwan; lcchang@mail.mcut.edu.tw

² Center for Thin Film Technologies and Applications, Ming Chi University of Technology, New Taipei City 24301, Taiwan

³ Institute of Materials Engineering, National Taiwan Ocean University, Keelung 20224, Taiwan; 10555014@ntou.edu.tw (Y.-Z.Z.); 10355009@ntou.edu.tw (S.-C.C.); 10555007@ntou.edu.tw (B.-W.L.)

* Correspondence: yichen@mail.ntou.edu.tw; Tel.: +886-2-2462-2192

Received: 15 April 2018; Accepted: 8 May 2018; Published: 11 May 2018



Abstract: High-Si-content transition metal nitride coatings, which exhibited an X-ray amorphous phase, were proposed as protective coatings on glass molding dies. In a previous study, the Zr–Si–N coatings with Si contents of 24–30 at.% exhibited the hardness of Si₃N₄, which was higher than those of the middle-Si-content (19 at.%) coatings. In this study, the bonding characteristics of the constituent elements of Zr–Si–N coatings were evaluated through X-ray photoelectron spectroscopy. Results indicated that the Zr 3d_{5/2} levels were 179.14–180.22 and 180.75–181.61 eV for the Zr–N bonds in ZrN and Zr₃N₄ compounds, respectively. Moreover, the percentage of Zr–N bond in the Zr₃N₄ compound increased with increasing Si content in the Zr–Si–N coatings. The Zr–N bond of Zr₃N₄ dominated when the Si content was >24 at.%. Therefore, high Si content can stabilize the Zr–N compound in the M₃N₄ bonding structure. Furthermore, the thermal stability and chemical inertness of Zr–Si–N coatings were evaluated by conducting thermal cycle annealing at 270 °C and 600 °C in a 15-ppm O₂–N₂ atmosphere. The results indicated that a Zr₂₂Si₂₉N₄₉/Ti/WC assembly was suitable as a protective coating against SiO₂–B₂O₃–BaO-based glass for 450 thermal cycles.

Keywords: bonding characteristics; chemical inertness; glass molding; mechanical properties; oxidation resistance

1. Introduction

Glass molding [1–3] has become a vital technique to fabricate aspherical lenses utilized as optical elements for image capture systems in cameras and mobile phones. Protective coatings on glass molding dies are crucial because molding processes are conducted at molding temperatures that are within the range of glass materials' softening points to deform the glass into the final lens shape [1]. Moreover, to be suitable for mass production, molding dies must endure a thermal cycle at temperatures ranging from room temperature to molding temperatures under high pressing loads. Therefore, the requirements of protective coatings are high hardness, smooth surface morphology, high thermal stability, adequate adhesion, long cyclability, and chemical inertness. Following the successful utilization of noble metal alloys [4–11] and carbon films [12,13], transition metal nitride films [14–23], which offer cost reduction and process control benefits, have become candidates for protective coatings. The oxidation resistance levels of some transition metal nitrides have been improved by the introduction of Si; in particular, improvements to Ti–Si–N [24–26] and Zr–Si–N [27–29] coatings have been reported. The improved oxidation resistance was attributed to the absence of

grain boundaries in the nitride coatings [30]. However, the advances in the oxidation resistance were accompanied by a decline in the mechanical properties due to the increase of amorphous volume. In our previous study [31], the nanoindentation hardness values of Zr–Si–N coatings with Si levels of 1–19 at.% increased initially with increasing Si content, peaked, and then dropped to lower levels for higher Si levels, which followed the typical mechanical characteristics of M–Si–N coatings (M: transition metal). However, the coatings with an Si level of 24–30 at.% exhibited the hardness level of Si_3N_4 , which was higher than that of the coatings with Si levels of 14–19 at.%. The broad reflection of the X-ray diffraction pattern of the amorphous phase located between standard ZrN (111) and orthorhombic Zr_3N_4 (320) suggested that high Si content can stabilize the nitride in the bonding structure of M_3N_4 . Therefore, exploring the coating constitutions, which are vital to the coatings' mechanical properties, is imperative. In this study, the effects of sputtering process variables, including the nitrogen flow ratio and substrate holder rotation speed, on the mechanical properties of coatings were investigated. Moreover, the bonding characteristics of the Zr–Si–N coatings with Si levels in the range of 0–30 at.% were examined through X-ray photoelectron spectroscopy. The correlation between the coating constitutions, structural characteristics, and mechanical properties was explored. Finally, the thermal stability and chemical inertness of Zr–Si–N coatings against heat effects and glass materials were evaluated.

2. Materials and Methods

Three batches of Zr–Si–N coatings were prepared on silicon and cemented carbide (WC–6 wt.%, CB-CERATIZIT, New Taipei City, Taiwan) substrates with dimensions of $20 \times 20 \times 0.525 \text{ mm}^3$ and $20 \times 20 \times 3.5 \text{ mm}^3$, respectively, at room temperature through reactive direct current magnetron cosputtering. The sputtering equipment and cosputtering processes were described in detail in a previous study [32]. As illustrated in our previous study [31], Batch I was prepared using various sputter powers. The main process variables for Batches II and III were the nitrogen flow ratio and substrate holder rotation speed, respectively. The evaluations on thermal stability and chemical inertness of Zr–Si–N coatings against SiO_2 – B_2O_3 – BaO -based glass plates (L-BAL42, Tg: 506 °C, Hk: 590, OHARA, Kanagawa, Japan) were conducted in a quartz tube furnace to simulate glass molding in thermal cycle annealing in a continuous flow of a 15-ppm O_2 – N_2 atmosphere. The glass plates with dimensions of $9.4 \times 9.26 \times 6.7 \text{ mm}^3$ were placed on the samples during thermal cycle annealing, which involves annealing at 270 °C and 600 °C and maintaining the glasses at $600 \text{ °C} \pm 10 \text{ °C}$ for 1 min/cycle [33]. The samples were removed from the furnace every 50 thermal cycles for surface observations using an optical microscope (OM, BX-51, Olympus, Tokyo, Japan).

Chemical composition analysis was conducted by using a field-emission electron probe microanalyzer (FE-EPMA, JXA-8500F, JEOL, Akishima, Japan) on the surface of the samples. The standard deviations for chemical composition data were calculated from 3 measurements made at different locations on one sample. Thickness evaluation on cross-sectional images of the coatings was performed by using a field emission scanning electron microscope (FE-SEM, S4800, Hitachi, Tokyo, Japan) at a 15-kV accelerating voltage. A conventional X-ray diffractometer (XRD, X'Pert PRO MPD, PANalytical, Almelo, The Netherlands) with $\text{Cu K}\alpha$ radiation was adopted to identify the phases of the coatings, using the grazing incidence technique with an incidence angle of 1° . The $\text{Cu K}\alpha$ radiation was generated from a Cu anode operated at 45 kV and 40 mA. The chemical states of the constituent elements were examined by using an X-ray photoelectron spectroscope (XPS, PHI 1600, PHI, Kanagawa, Japan) with an $\text{Mg K}\alpha$ X-ray beam (energy = 1253.6 eV and power = 250 W) operated at 15 kV. The XPS spectra of N 1s, Si 2p, and Zr 3d core levels were recorded. Ar^+ ion beam of 3 keV was used to sputter the coatings for depth profiling. The nonlinear least squares curve fittings were conducted to deconvolute the spectra. The backgrounds were corrected by using a Shirley function and the peaks were fitted by using Gaussian–Lorentzian functions. To split the $3d_{5/2}$ – $3d_{3/2}$ Zr doublets, the $I(3d_{5/2}):I(3d_{3/2})$ intensity ratio was set to 3:2 because of spin-orbit splitting. The splitting energies were 2.43 eV for Zr 3d doublets [34]. The surface nanoindentation hardness and Young's

modulus of coatings were measured with a nanoindentation tester (TI-900 Triboindenter, Hysitron, Minneapolis, MN, USA). The nanoindenter (TI-0039, Hysitron, Minneapolis, MN, USA) was equipped with a Berkovich diamond probe tip, whose radius was 200 nm in diameter. The applied load was controlled to produce an indentation depth of 80 nm. The loading, holding, and unloading times were 5 s each. The nanoindentation hardness and elastic modulus of each indent were calculated using the Oliver and Pharr method [35]. The standard deviations for hardness and elastic modulus data were calculated from 5 measurements made at different locations on one sample. The surface roughness values of the coatings, R_a [36], were evaluated by using an atomic force microscope (AFM, Dimension 3100 SPM, NanoScope IIIa, Veeco, Santa Barbara, CA, USA). The scanning area of each image was set at $5 \times 5 \mu\text{m}^2$ with a scanning rate of 1.0 Hz. The residual stress of the films measured by the curvature method was calculated using Stoney's equation [37].

$$\sigma_f t_f = \frac{E_S h_S^2}{6(1 - \nu_S) R_f} \quad (1)$$

where σ_f is the in-plane stress component in the film, t_f is the thickness of the film, E_S is the Young's modulus of the Si substrate (130.2 GPa), ν_S is the Poisson's ratio for the Si substrate (0.279) [38], h_S is the thickness of the substrate (525 μm), and R_f is the radius of the curvature of the film. The measurements were calibrated using BK7 glass plates with curvatures of 0, -0.1 , and $+0.1 \text{ m}^{-1}$; the deviation was 10%. The curvature measurements were conducted using a scan of 10 nm on the surface by recording the reflection of a laser beam. Each sample was analyzed 10 times in each of the two perpendicular directions.

3. Results and Discussion

3.1. As-Deposited Zr–Si–N Coatings

Table 1 lists the sputtering variables, chemical compositions, and thicknesses of the Zr–Si–N coatings prepared in this study. The sputtering times were controlled to deposit coatings with thicknesses ranging from 890 to 1080 nm; therefore the indentation depth of 80 nm fitted the 1/10 rule for determining the mechanical properties of the coatings. The oxygen contents in the Zr–Si–N coatings were 0.8–1.1 at.%. The samples could be designated in the form $\text{Zr}_x\text{Si}_y\text{N}_{(100-x-y)}$ (f,Rx), where f is the $(\text{N}_2/(\text{N}_2 + \text{Ar}))$ flow ratio and Rx is the substrate holder rotation speed (x rpm) in the sputtering process. Figure 1 illustrates the XRD patterns of the as-deposited Batch-II Zr–Si–N coatings prepared using sputter powers of $W_{\text{Zr}} = 100 \text{ W}$ and $W_{\text{Si}} = 100 \text{ W}$, a substrate holder rotation speed of 5 rpm, and various $(\text{N}_2/(\text{N}_2 + \text{Ar}))$ flow ratios ranging from 0.1 to 0.5. All the Batch II Zr–Si–N coatings with a high Si content of 30–33 at.% exhibited an X-ray amorphous phase and similar chemical compositions. The deposition rate decreased from 10.8, to 8.8, to 7.2, to 6.1, and to 5.1 nm/min as the $(\text{N}_2/(\text{N}_2 + \text{Ar}))$ flow ratio was increased from 0.1, to 0.2, to 0.3, to 0.4, and to 0.5, respectively. Moreover, the Batch III Zr–Si–N coatings prepared using sputter powers of $W_{\text{Zr}} = 100 \text{ W}$ and $W_{\text{Si}} = 100 \text{ W}$, a substrate holder rotation speed of 1–30 rpm, and a $(\text{N}_2/(\text{N}_2 + \text{Ar}))$ flow ratio of 0.4 also exhibited similar chemical compositions (31–37 at.% Si), a deposition rate of 5.9–6.9 nm/min, and an X-ray amorphous phase (not discussed in this paper). Figure 2 illustrates the ternary diagram of the phase distribution of all the Zr–Si–N coatings, including the Batch I coatings prepared using various sputtering powers, a substrate holder rotation speed of 5 rpm, and a $(\text{N}_2/(\text{N}_2 + \text{Ar}))$ flow ratio of 0.4, as described in our previous study [31]. These coatings were classified into three phase types: face-centered cubic (f.c.c.), amorphous, and f.c.c. and amorphous mixed phases.

Table 1. Sputtering parameters, chemical compositions, thicknesses, mechanical properties, and residual stresses of Zr–Si–N coatings.

Sample	Sputtering Power (W)		N ₂ Ratio	R ¹	Time	Chemical Composition (at.%)				T ²	H ³	E ⁴	Residual Stress
	W _{Zr}	W _{Si}				Zr	Si	N	O				
Batch I													
Zr ₆₀ N ₄₀	300	0	0.4	5	60	57.9 ± 0.8	–	38.8 ± 0.8	3.3 ± 0.1	820	21.0 ± 0.3	248 ± 6	−0.9 ± 0.2
Zr ₅₈ Si ₂ N ₄₀	290	10	0.4	5	60	56.9 ± 1.0	1.8 ± 0.2	39.0 ± 1.2	2.3 ± 0.3	860	23.6 ± 0.4	267 ± 4	−1.2 ± 0.1
Zr ₅₄ Si ₆ N ₄₀	280	20	0.4	5	70	53.5 ± 0.7	5.9 ± 0.1	39.3 ± 1.0	1.3 ± 0.3	680	19.7 ± 0.2	204 ± 3	−1.7 ± 0.1
Zr ₅₂ Si ₈ N ₄₀	270	30	0.4	5	70	51.2 ± 1.4	8.1 ± 0.1	39.7 ± 1.7	1.0 ± 0.2	700	18.4 ± 0.2	207 ± 2	−1.0 ± 0.3
Zr ₄₄ Si ₁₄ N ₄₂	235	65	0.4	5	70	43.8 ± 1.1	13.7 ± 0.3	41.5 ± 1.3	1.0 ± 0.2	740	13.4 ± 0.1	191 ± 4	0.4 ± 0.2
Zr ₃₅ Si ₁₅ N ₅₀	225	75	0.4	5	70	34.3 ± 0.7	14.7 ± 0.3	49.3 ± 0.9	1.7 ± 0.1	811	13.8 ± 0.2	187 ± 3	0.1 ± 0.3
Zr ₃₄ Si ₁₉ N ₄₇	200	100	0.4	5	80	33.9 ± 0.4	18.8 ± 0.4	45.9 ± 0.8	1.4 ± 0.1	940	11.7 ± 0.7	148 ± 5	0.2 ± 0.1
Zr ₂₈ Si ₂₄ N ₄₈	150	150	0.4	5	90	28.0 ± 0.5	23.8 ± 0.3	47.2 ± 0.6	1.0 ± 0.2	840	13.7 ± 0.4	196 ± 2	0.2 ± 0.1
Zr ₂₂ Si ₃₀ N ₄₈	100	100	0.4	5	150	21.6 ± 0.2	29.4 ± 0.3	48.2 ± 0.4	0.8 ± 0.2	910	16.2 ± 0.4	217 ± 4	−0.3 ± 0.0
Batch II													
Zr ₂₄ Si ₃₀ N ₄₆	100	100	0.1	5	100	23.4 ± 0.3	30.1 ± 0.2	45.7 ± 0.5	0.9 ± 0.1	1080	14.7 ± 0.4	210 ± 5	−0.1 ± 0.1
Zr ₂₁ Si ₃₁ N ₄₈	100	100	0.2	5	120	20.8 ± 0.2	30.4 ± 0.3	47.8 ± 0.5	1.0 ± 0.0	1050	14.4 ± 0.4	209 ± 7	0.2 ± 0.2
Zr ₂₂ Si ₃₀ N ₄₈	100	100	0.3	5	140	21.7 ± 0.1	30.3 ± 0.3	47.2 ± 0.4	0.9 ± 0.0	1010	15.1 ± 0.4	215 ± 5	0.0 ± 0.1
Zr ₂₂ Si ₃₀ N ₄₈	100	100	0.4	5	150	21.6 ± 0.2	29.4 ± 0.3	48.2 ± 0.4	0.8 ± 0.2	910	16.2 ± 0.4	217 ± 4	−0.3 ± 0.0
Zr ₂₃ Si ₃₃ N ₄₄	100	100	0.5	5	180	22.5 ± 0.3	32.6 ± 0.7	43.8 ± 0.9	1.1 ± 0.1	920	18.4 ± 0.4	237 ± 5	−0.5 ± 0.1
Batch III													
Zr ₂₀ Si ₃₆ N ₄₄	100	100	0.4	1	150	20.3 ± 0.4	35.3 ± 0.3	43.4 ± 0.4	1.1 ± 0.1	950	15.6 ± 0.3	212 ± 6	−0.5 ± 0.3
Zr ₂₄ Si ₃₁ N ₄₅	100	100	0.4	3	150	23.6 ± 0.3	31.0 ± 0.5	44.4 ± 1.0	1.0 ± 0.1	1033	15.0 ± 0.5	208 ± 5	−0.2 ± 0.1
Zr ₂₄ Si ₃₁ N ₄₅	100	100	0.4	7	150	23.5 ± 0.3	30.8 ± 0.4	44.6 ± 0.8	1.1 ± 0.1	1040	15.2 ± 0.2	205 ± 7	−0.1 ± 0.1
Zr ₂₀ Si ₃₅ N ₄₅	100	100	0.4	10	150	19.8 ± 0.3	34.7 ± 0.2	44.6 ± 0.2	0.9 ± 0.1	920	16.1 ± 0.2	206 ± 4	−0.4 ± 0.3
Zr ₂₀ Si ₃₇ N ₄₃	100	100	0.4	20	150	20.2 ± 0.4	36.2 ± 0.4	42.7 ± 0.8	0.9 ± 0.0	905	15.1 ± 0.2	194 ± 5	−0.5 ± 0.1
Zr ₂₁ Si ₃₅ N ₄₄	100	100	0.4	30	150	20.6 ± 0.5	34.5 ± 0.8	43.7 ± 1.2	1.1 ± 0.4	890	15.8 ± 0.2	211 ± 6	−0.3 ± 0.2

Notes: ¹ R: Rotation speed. ² T: Thickness. ³ H: Hardness. ⁴ E: Young's modulus.

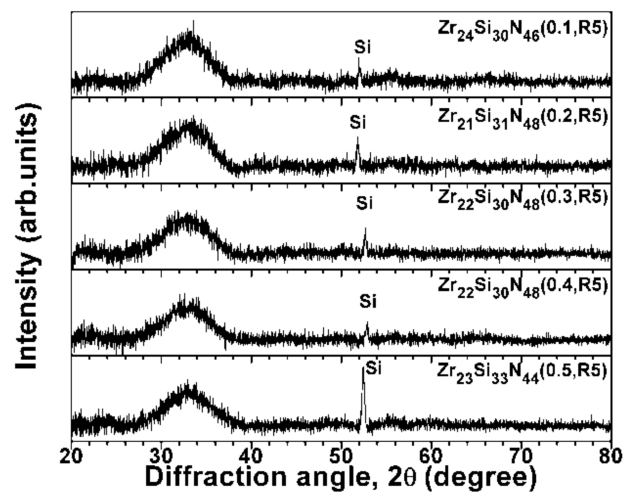


Figure 1. XRD patterns of as-deposited Zr-Si-N coatings prepared on Si substrates using various $(N_2/(N_2 + Ar))$ flow ratios, a substrate holder rotation speed of 5 rpm, and sputter powers of $W_{Zr} = 100$ W and $W_{Si} = 100$ W.

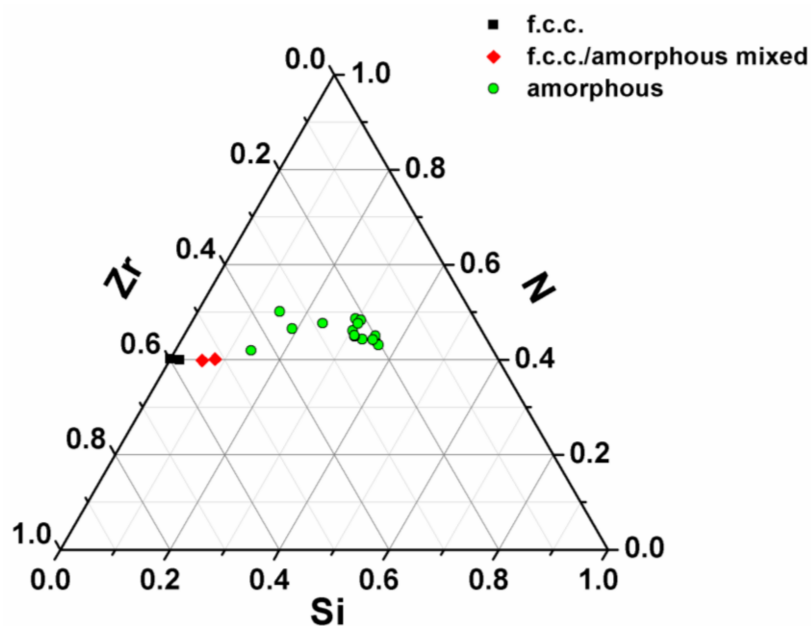


Figure 2. Phase distribution of Zr-Si-N coatings.

Figure 3a shows the relationship between the nanoindentation hardness and residual stress of the Zr-Si-N coatings. In each of the three coating types, the nanoindentation hardness levels exhibited decreasing tendencies as the residual stress varied from compressive toward tensile. Figure 3b shows the relationship between the nanoindentation hardness and Si content of the Zr-Si-N coatings; these X-ray amorphous-phase coatings with a high Si content of 30–37 at.% exhibited a high hardness level, which was similar to that of X-ray amorphous-phase coatings with an Si content of 14–24 at.%. The bonding characteristics of the X-ray amorphous-phase coatings exhibiting divergent mechanical properties were further analyzed. Because the hardness levels of the moldable optical glasses ranged from 3.2 to 7.0 GPa, the protective coatings on the glass molding dies exhibiting a hardness level higher than 10 GPa were preferred [10]. Therefore, Zr-Si-N coatings with a high Si content of 30 at.% exhibiting nanoindentation hardness higher than 14.4 GPa should be suitable for protective coatings.

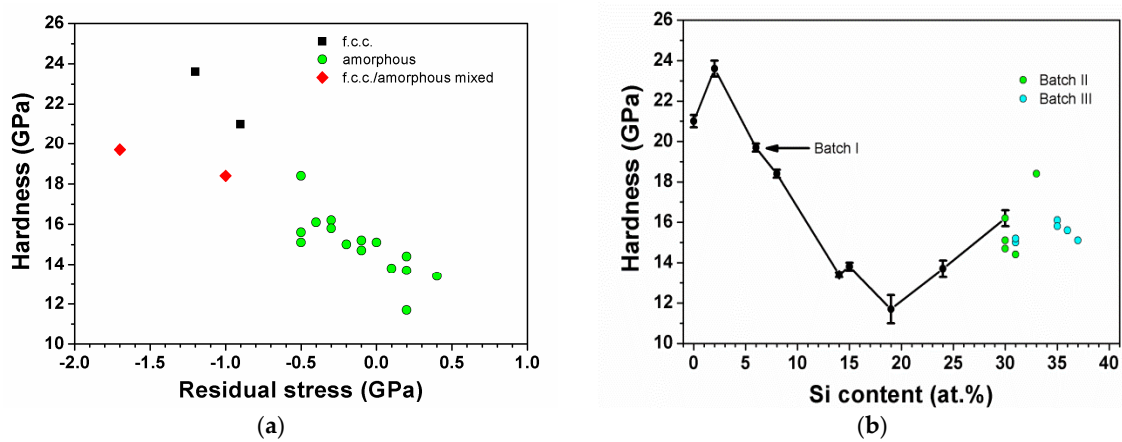


Figure 3. Relationships between nanoindentation hardness and (a) residual stress and (b) Si content of Zr-Si-N coatings.

3.2. XPS Study of Zr-Si-N Coatings

In a previous study [31], the low-Si-content (0–2 at.%) Zr-Si-N coatings exhibited an f.c.c. structure, whereas the medium-Si-content (6–8 at.%) coatings exhibited a mixture of f.c.c. and amorphous phases, and the high-Si-content (14–37 at.%) coatings exhibited X-ray amorphous structures. Figure 4 shows the XRD reflections of $Zr_{58}Si_2N_{40}(0.4,R5)$, $Zr_{52}Si_8N_{40}(0.4,R5)$, and $Zr_{22}Si_{30}N_{48}(0.4,R5)$ coatings, respectively representing the aforementioned three classifications. Figure 5 shows the XPS depth profiles of Zr 3d, Si 2p, and N 1s core levels of the as-deposited $Zr_{22}Si_{30}N_{48}(0.4,R5)$ coatings. The profiles of each element at a depth range of 10–70 nm were similar, whereas the profiles on the free surface exhibited deviations caused by the contamination from O. The oxygen content of the as-deposited $Zr_{22}Si_{30}N_{48}(0.4,R5)$ coatings was 0.8 at.%, examined from the surface of the samples by using an FE-EPMA. Figure 6a shows a curve fitting of the Zr profile at a depth of 60 nm of the $Zr_{22}Si_{30}N_{48}(0.4,R5)$ coatings; the Zr profile was split into two sets of doublets, representing Zr-N bonds for two compounds, ZrN and Zr_3N_4 . The Zr 3d_{5/2} signals were determined at 180.22 ± 0.03 and 181.01 ± 0.06 eV for ZrN and Zr_3N_4 , respectively, which exhibited a count ratio of 46:54. Figure 6b,c show the curve fitting of the Zr profiles at a depth of 60 nm of the $Zr_{52}Si_8N_{40}(0.4,R5)$ and $Zr_{58}Si_2N_{40}(0.4,R5)$ coatings, respectively; ZrN was the dominant Zr compound. The Zr 3d_{5/2} signals were 179.14 and 181.09 eV for ZrN and Zr_3N_4 in the $Zr_{52}Si_8N_{40}(0.4,R5)$ coatings, respectively, whereas these signals were 179.30 and 181.61 eV for ZrN and Zr_3N_4 in the $Zr_{58}Si_2N_{40}(0.4,R5)$ coatings, respectively.

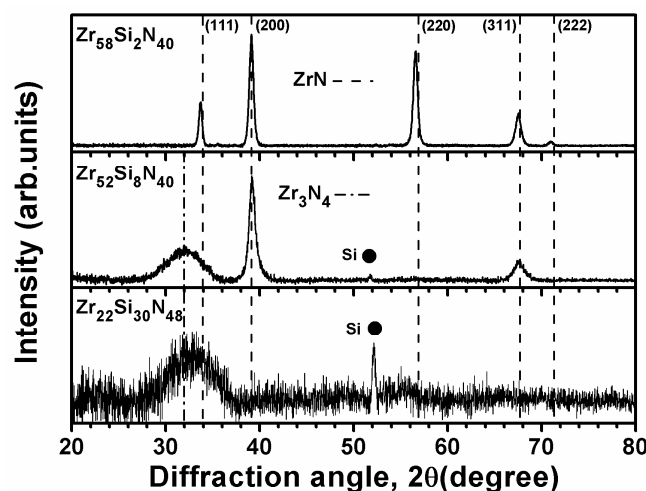


Figure 4. XRD patterns of $Zr_{58}Si_2N_{40}(0.4,R5)$, $Zr_{52}Si_8N_{40}(0.4,R5)$, and $Zr_{22}Si_{30}N_{48}(0.4,R5)$ coatings.

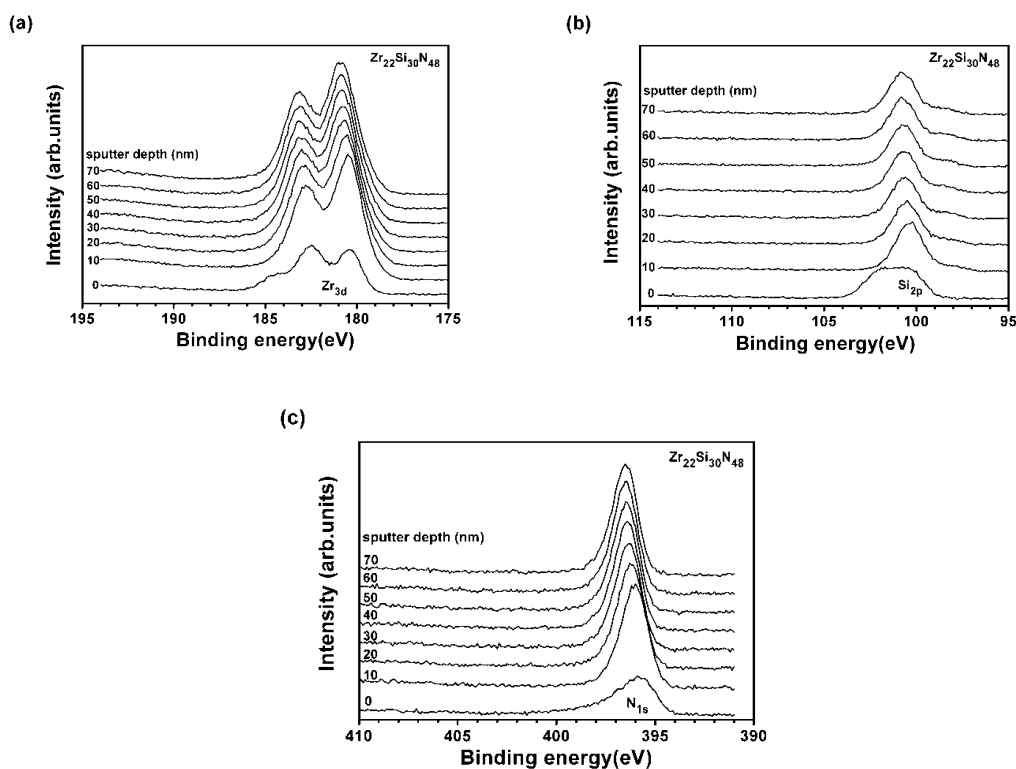


Figure 5. XPS depth profiles of (a) Zr 3d; (b) Si 2p; and (c) N 1s of $Zr_{22}Si_{30}N_{48}(0.4,R5)$ coatings.

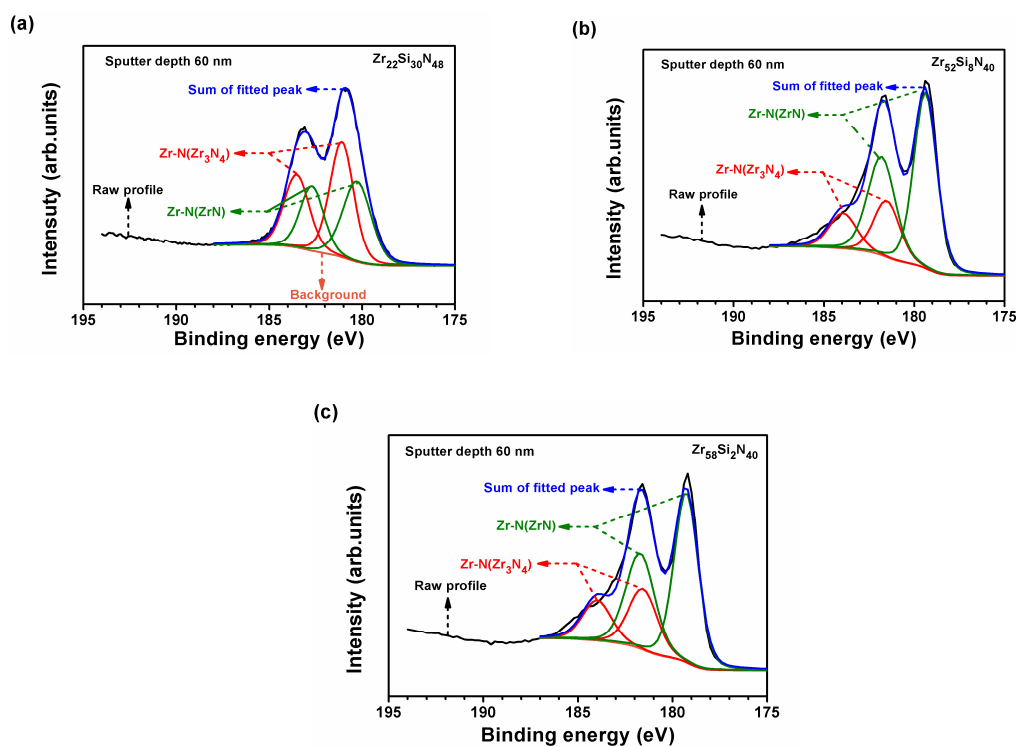


Figure 6. XPS profiles of Zr 3d core levels of (a) $Zr_{22}Si_{30}N_{48}(0.4,R5)$; (b) $Zr_{52}Si_8N_{40}(0.4,R5)$; and (c) $Zr_{58}Si_2N_{40}(0.4,R5)$ coatings at a depth of 60 nm.

Table 2 lists all the binding energies for the bonds from ZrN, Zr₃N₄, and Si₃N₄ compounds in the Zr–Si–N coatings. The binding energies of Zr 3d_{5/2} related to Zr–N bonds for ZrN and Zr₃N₄ compounds were in the range of 179.14–180.22 and 180.75–181.61 eV, respectively, which were comparable to the reported values of 179.6 eV for ZrN_x and 181.0 eV for ZrN_{1+x} [39]. Figure 7a shows that the Si 2p of Zr₂₂Si₃₀N₄₈(0.4,R5) coatings comprised two signals, 98.51 ± 0.11 and 100.59 ± 0.13 eV for free Si and Si–N bonds, respectively. The Si substrate without the aforementioned coatings exhibited a Si 2p signal of 99.35 ± 0.01 eV. Choi et al. [25] reported that free Si at a binding energy of 99.3 eV was observed for Ti–Si–N coatings with an Si content >17 at.% because of the deficiency of N. Figure 7b shows that the Si 2p of Zr₅₂Si₈N₄₀(0.4,R5) coatings comprised 98.92 and 100.68 eV signals for free Si and Si–N bonds, respectively. Because the Si content was 2 at.% only for the Zr₅₈Si₂N₄₀(0.4,R5) coatings, the Si signal was undetectable because of the analysis limitation. The binding energies of Si 2p related to free Si and Si–N bonds for Si₃N₄ compound were in the range of 98.41–98.92 and 100.59–100.89 eV, respectively. The latter value exhibited a lower correlation to the reported value of 102.0 eV for Zr₃N₄ film [39]. Figure 8 shows that N 1s of Zr₂₂Si₃₀N₄₈(0.4,R5) coatings comprised signals of 396.97 ± 0.11, 396.13 ± 0.12, and 397.94 ± 0.18 eV for N–Zr bond in ZrN, N–Zr bond in Zr₃N₄, and N–Si bond in Si₃N₄, respectively. The binding energies of N 1s of all the Zr–Si–N coatings related to N–Zr in ZrN, N–Zr in Zr₃N₄, and N–Si in Si₃N₄ were in the range of 396.87–397.05, 396.03–396.20, and 397.94–398.58 eV, respectively, which were higher than the reported values of 396.3, 395.4, and 397.7 eV [39].

Table 2. Binding energies of Zr–Si–N(0.4,R5) coatings.

Sample	Binding Energy (eV)						
	Zr _{3d 5/2}		Si _{2p}		N _{1s}		
	ZrN	Zr ₃ N ₄	Si ₃ N ₄	Free Si	ZrN	Zr ₃ N ₄	Si ₃ N ₄
Zr ₆₀ N ₄₀	179.55 ± 0.06	181.39 ± 0.05	–	–	397.05 ± 0.03	396.20 ± 0.05	–
Zr ₅₈ Si ₂ N ₄₀	179.30 ± 0.03	181.61 ± 0.02	–	–	396.87 ± 0.01	396.06 ± 0.05	398.58 ± 0.16
Zr ₅₃ Si ₈ N ₃₉	179.14 ± 0.04	181.09 ± 0.06	100.68 ± 0.08	98.92 ± 0.48	396.90 ± 0.01	396.03 ± 0.01	398.36 ± 0.29
Zr ₄₄ Si ₁₄ N ₄₂	179.51 ± 0.01	180.93 ± 0.02	100.67 ± 0.06	98.53 ± 0.15	396.98 ± 0.01	396.12 ± 0.10	398.53 ± 0.10
Zr ₃₄ Si ₁₉ N ₄₇	179.44 ± 0.00	180.75 ± 0.03	100.68 ± 0.02	98.41 ± 0.09	396.94 ± 0.05	396.08 ± 0.02	398.31 ± 0.18
Zr ₂₈ Si ₂₄ N ₄₈	179.87 ± 0.07	181.03 ± 0.04	100.89 ± 0.05	98.74 ± 0.06	397.04 ± 0.03	396.18 ± 0.03	398.21 ± 0.17
Zr ₂₂ Si ₃₀ N ₄₈	180.22 ± 0.03	181.01 ± 0.06	100.59 ± 0.13	98.51 ± 0.11	396.97 ± 0.11	396.13 ± 0.12	397.94 ± 0.18

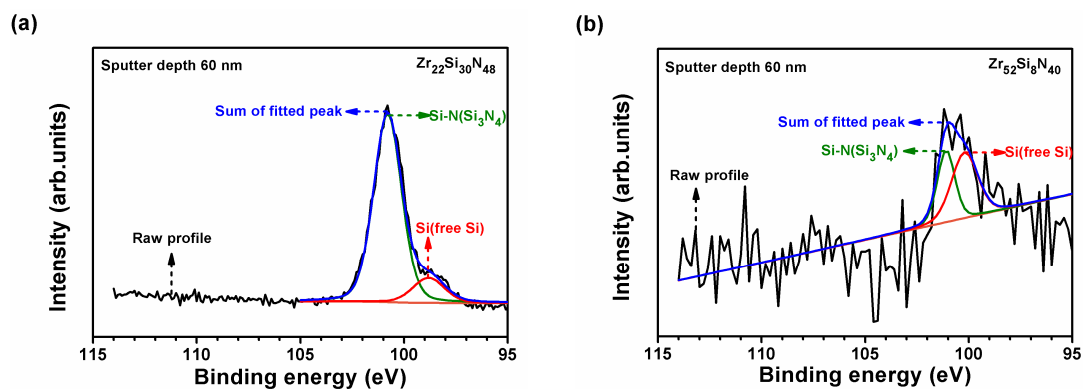


Figure 7. XPS profiles of Si 2p core levels of (a) Zr₂₂Si₃₀N₄₈(0.4,R5) and (b) Zr₅₂Si₈N₄₀(0.4,R5) coatings at a depth of 60 nm.

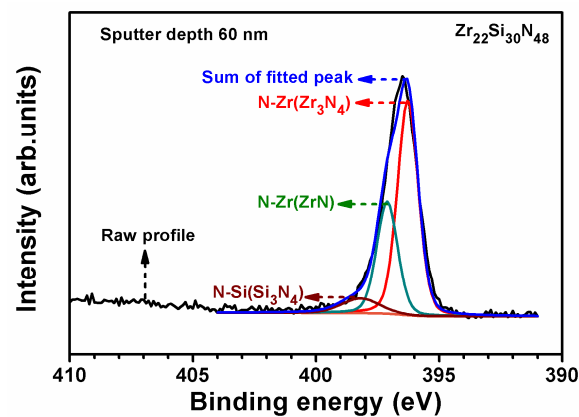


Figure 8. XPS profiles of N 1s core levels of $Zr_{22}Si_{30}N_{48}(0.4,R5)$ coatings at a depth of 60 nm.

Figure 9 shows the variations in bond characteristics for various Si levels of Zr–Si–N(0.4,R5) coatings. Figure 9a,c show that Zr and N were likely to form a Zr_3N_4 compound as the Si content in the coatings increased, whereas Si formed Si–N bonds with increasing Si content in the coatings (Figure 9b). Thus, the bond characteristics of $Zr_{28}Si_{24}N_{48}(0.4,R5)$ and $Zr_{22}Si_{30}N_{48}(0.4,R5)$ coatings are Zr_3N_4 - and Si_3N_4 -dominated; therefore, the Zr–Si–N coatings with higher Si content of 24–30 at.% exhibited the hardness of Si_3N_4 at 18–19 GPa [40–42].

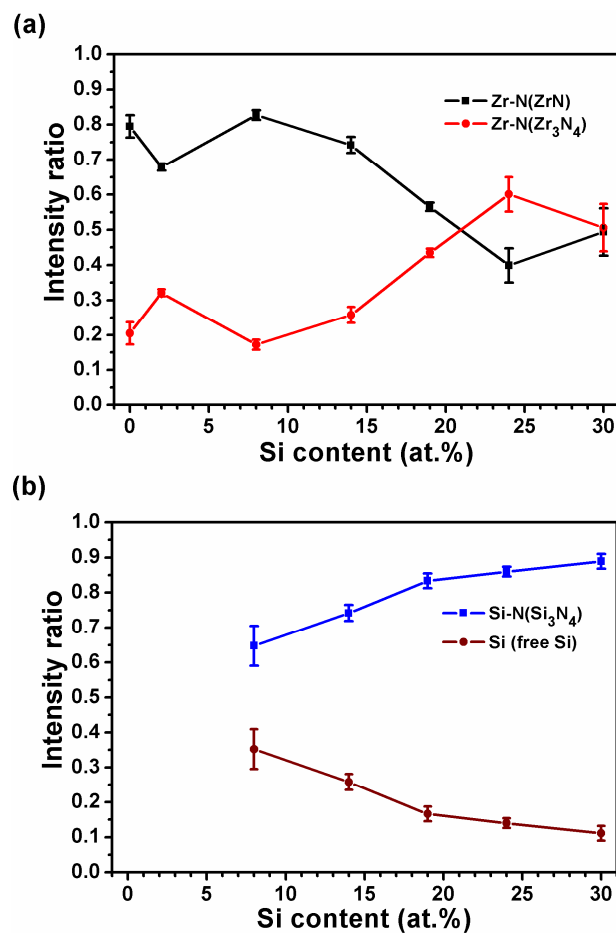


Figure 9. Cont.

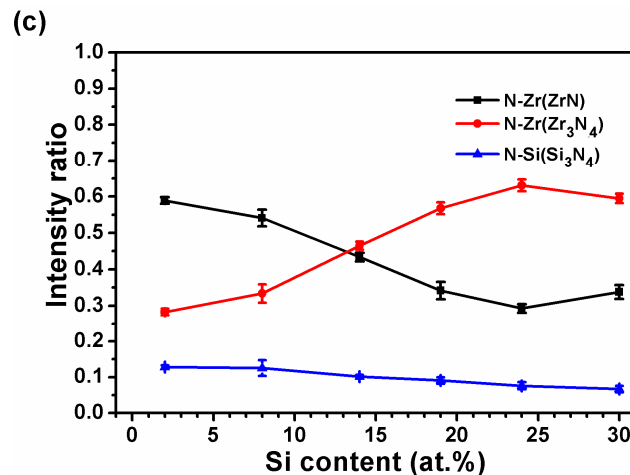


Figure 9. XPS signal ratios of (a) Zr; (b) Si; and (c) N of Zr–Si–N(0.4,R5) coatings.

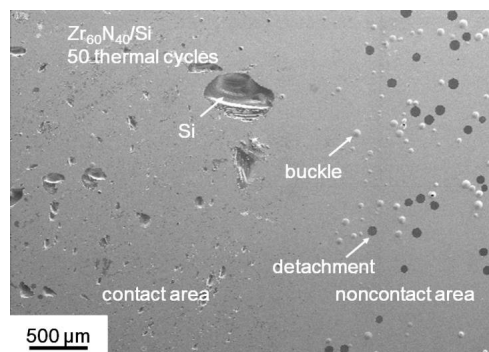
3.3. Thermal Stability and Chemical Inertness of Zr–Si–N Coatings

In our previous study [31], high-Si-content (15–30 at.%) Zr–Si–N(0.4,R5) coatings exhibited oxidation resistance levels superior to those of low- and medium-Si-content coatings through examination of their oxide layer thicknesses after they were annealed at 600 °C in 1% O₂–99% Ar for up to 100 h. The improvement of oxidation resistance was attributed to the formation of amorphous Si–Zr–O oxide scales, which were restricted following oxygen diffusion; thus, the mechanical properties of the high-Si-content (15–30 at.%) Zr–Si–N coatings were similar to those of as-deposited coatings. In the glass molding process, the molded products transfer the surface quality (figure and roughness) from the molding dies. Therefore, a coating roughness maintained at a nanoscale over a long lifetime is preferred. Table 3 shows the surface roughness variations of Zr–Si–N(0.4,R5) coatings during thermal cycle annealing (270–600 °C) in a realistic molding atmosphere (15-ppm O₂–N₂). The inner positions of the coatings indicated the area contacted SiO₂–B₂O₃–BaO-based glass plates during thermal cycle annealing. The chemical inertness of the coatings against glass was evaluated by the presence of surface damage, such as scraps or dips [10], and flaked or island oxides [21], which consecutively result in roughness variation. The surface roughness variations on the outer positions indicated the thermal stability of the coatings during the glass molding process. The as-deposited Zr–Si–N(0.4,R5) coatings prepared on Si substrates exhibited a surface roughness of 0.3–1.0 nm. The surfaces of the outer positions (noncontact area in Figure 10) of low-Si-content Zr₆₀N₄₀(0.4,R5) and Zr₅₈Si₂N₄₀(0.4,R5) coatings exhibited severely circular buckle formation following detachment after 50 thermal cycles, whereas black dips exposing the Si substrate were observed in the inner positions (contact area in Figure 10), which implied sticking and detachment. The Zr₅₂Si₈N₄₀(0.4,R5) and Zr₄₄Si₁₄N₄₂(0.4,R5) coatings exhibited similar dips in the contact area after 50 thermal cycles, whereas a low surface roughness level of 0.4–0.7 nm was maintained in the noncontact area after 250 cycles. The Zr₃₅Si₁₅N₅₀(0.4,R5) and Zr₃₄Si₁₉N₄₇(0.4,R5) coatings exhibited dips in the contact area after 250 thermal cycles, whereas a low surface roughness level of 0.6–0.7 nm was maintained in their noncontact area after 250 cycles. Undetached parts of the contact area of the Zr₃₅Si₁₅N₅₀(0.4,R5) and Zr₃₄Si₁₉N₄₇(0.4,R5) coatings exhibited roughness values of 4.0 and 2.1 nm, respectively. The Zr₂₈Si₂₄N₄₈(0.4,R5) coatings maintained a smooth surface in the contact and noncontact areas after 250 cycles; however, dips occurred after 500 thermal cycles even though the surface roughness levels of the undetached part of the contact area and the noncontact area were 0.7 and 0.5 nm, respectively. For the amorphous Zr–Si–N(0.4,R5) coatings (14–24 at.% Si), a low surface roughness level of 0.5–0.7 nm was maintained in the noncontact area after 750 cycles. Therefore, the X-ray amorphous-phase Zr–Si–N coatings exhibited high thermal stability in the glass molding process, but their chemical inertness was relatively insufficient.

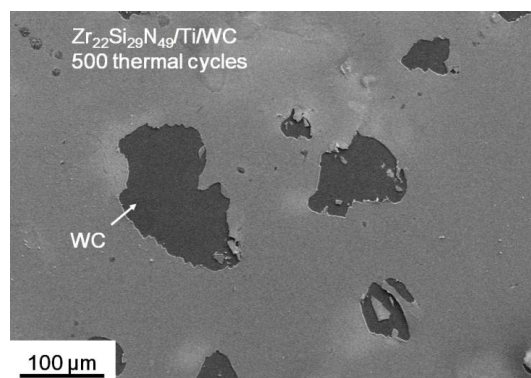
Table 3. Surface roughness variations of Zr–Si–N(0.4,R5) coatings after thermal cycle annealing.

Sample	Cycles	Surface Roughness (nm)							
		0	250	250	400	400	500	500	750
		Position	Inner ¹	Outer ²	Inner	Outer	Inner	Outer	Outer
Zr ₆₀ N ₄₀ /Si		1.0 ± 0.0	F ³	–	–	–	–	–	–
Zr ₅₈ Si ₂ N ₄₀ /Si		0.9 ± 0.1	F	–	–	–	–	–	–
Zr ₅₃ Si ₈ N ₃₉ /Si		0.3 ± 0.0	F	0.4 ± 0.1	–	–	–	2.0 ± 0.3	11 ± 0.5
Zr ₄₄ Si ₁₄ N ₄₂ /Si		0.5 ± 0.0	F	0.7 ± 0.0	–	–	–	0.5 ± 0.0	0.6 ± 0.0
Zr ₃₅ Si ₁₅ N ₅₀ /Si		0.6 ± 0.0	F	0.7 ± 0.0	–	–	–	0.6 ± 0.0	0.6 ± 0.0
Zr ₃₄ Si ₁₉ N ₄₇ /Si		0.5 ± 0.0	F	0.6 ± 0.0	–	–	–	0.5 ± 0.0	0.5 ± 0.1
Zr ₂₈ Si ₂₄ N ₄₈ /Si		0.6 ± 0.0	0.8 ± 0.1	0.5 ± 0.0	–	–	F	0.5 ± 0.0	0.7 ± 0.1
Zr ₂₂ Si ₂₉ N ₄₉ /Ti/WC		1.5 ± 0.0	1.5 ± 0.1	1.4 ± 0.0	1.8 ± 0.2	1.8 ± 0.1	F	1.8 ± 0.1	–

Notes: ¹ inner: The area contact glass plate; ² outer: The area outside the contact area; ³ F: Failure.

**Figure 10.** Surface morphology of the Zr₆₀N₄₀(0.4,R5)/Si assembly after 50 thermal cycles.

Cemented carbide is a representative die material for glass molding. A Ti interlayer of 100 nm was inserted to fabricate the Zr–Si–N/Ti/WC assembly, which prevented buckle formation during repeated thermal cycle annealing [21]. The Zr₂₂Si₃₀N₄₈(0.4,R5) process was conducted again to fabricate a Zr₂₂Si₂₉N₄₉/Ti/WC assembly; this assembly exhibited a surface roughness of 1.5 nm in the as-deposited state, which was higher than those of the Zr–Si–N(0.4,R5) coatings prepared on Si wafers. The Zr₂₂Si₂₉N₄₉/Ti/WC assembly maintained a smooth surface in the contact and noncontact areas after 250 and 400 thermal cycles; however, black dips of the Zr₂₂Si₂₉N₄₉/Ti coatings occurred after 500 thermal cycles (Figure 11). No buckle formation was observed. The 450-cycle-treated sample showed no sticking marks. The as-prepared Zr₂₂Si₂₉N₄₉/Ti/WC assembly exhibited a surface roughness of 1.5 nm, which was lower than that of the Ta₂₆Si₁₆N₅₈/Ti/WC assembly (2.9 nm), indicating a higher chemical inertness of 1400 thermal cycles against SiO₂–B₂O₃–BaO-based glass [21].

**Figure 11.** Surface morphology of the contact area of the Zr₂₂Si₂₉N₄₉/Ti/WC assembly after 500 thermal cycles.

4. Conclusions

The Zr–Si–N coatings with an Si content higher than 14 at.% exhibited an X-ray amorphous phase. Moreover, the nanoindentation hardness level of the Zr–Si–N coatings with an Si content of >30 at.% was >14.4 GPa, which was higher than those of the coatings with an Si content of 14–24 at.%; this was attributed to the variation of bonding characteristics. The structure varied from crystalline ZrN-dominant to amorphous Zr₃N₄-dominant with increasing Si content in the Zr–Si–N coatings. The bond characteristics of Zr₂₈Si₂₄N₄₈ and Zr₂₂Si₃₀N₄₈ coatings exhibited a Zr₃N₄- and Si₃N₄-dominated nitride structure, and the nanoindentation hardness values were approximately similar to that of Si₃N₄. Buckle formation and the sticking effect became major disadvantages for protective coatings during the glass molding process. The Zr₂₂Si₂₉N₄₉/Ti/WC assembly was suitable as a protective coating against SiO₂–B₂O₃–BaO-based glass for annealing for 450 thermal cycles at 270 °C and 600 °C in a 15-ppm O₂–N₂ atmosphere. Reducing the surface roughness by introducing an interlayer in the protective coating assembly and increasing the chemical inertness of the protective coatings are major concerns to be addressed in the future.

Author Contributions: L.-C.C. and Y.-I.C. conceived and designed the experiments; Y.-Z.Z. and S.-C.C. performed the coating experiments; Y.-Z.Z. and B.-W.L. performed the annealing experiments; Y.-Z.Z. and B.-W.L. analyzed the XPS data; Y.-I.C. wrote the paper.

Funding: This research was funded by the Ministry of Science and Technology, Taiwan (105-2221-E-019-007-MY3 and 106-2221-E-131-002).

Conflicts of Interest: The authors declare no conflict of interest. The founding sponsors had no role in the design of the study; in the collection, analyses, or interpretation of data; in the writing of the manuscript, and in the decision to publish the results.

References

1. Katsuki, M. Transferability of glass lens molding. *Proc. SPIE* **2006**, *6149*, 61490M.
2. Maschmeyer, R.O.; Andrysick, C.A.; Geyer, T.W.; Meissner, H.E.; Parker, C.J.; Sanford, L.M. Precision molded-glass optics. *Appl. Opt.* **1983**, *22*, 2410–2412. [[CrossRef](#)] [[PubMed](#)]
3. Yi, A.Y.; Jain, A. Compression molding of aspherical glass lenses—A combined experimental and numerical analysis. *J. Am. Ceram. Soc.* **2005**, *88*, 579–586. [[CrossRef](#)]
4. Monji, H.; Aoki, M.; Torii, H.; Okinaka, H. Molding Method for Producing Optical Glass Element. U.S. Patent 4,629,487A, 16 December 1986.
5. Kuribayashi, K.; Sakai, M.; Monji, H.; Aoki, M.; Okinaka, H.; Torii, H. Mold for Press-Molding Glass Optical Elements and a Molding Method Using the Same. U.S. Patent 4,685,948A, 11 August 1987.
6. Wu, F.B.; Chen, W.Y.; Duh, J.G.; Tsai, Y.Y.; Chen, Y.I. Ir-based multi-component coating on tungsten carbide by RF magnetron sputtering process. *Surf. Coat. Technol.* **2003**, *163–164*, 227–232. [[CrossRef](#)]
7. Klocke, F.; Bouzakis, K.D.; Georgiadis, K.; Gerardis, S.; Skordaris, G.; Pappa, M. Adhesive interlayers' effect on the entire structure strength of glass molding tools' Pt–Ir coatings by nano-tests determined. *Surf. Coat. Technol.* **2011**, *206*, 1867–1872. [[CrossRef](#)]
8. Chao, C.L.; Huo, C.B.; Chou, W.C.; Lin, Y.R.; Ma, K.J.; Chien, H.H. Study on the design of precious metal based protective films for glass moulding process. *Surf. Coat. Technol.* **2013**, *231*, 567–572. [[CrossRef](#)]
9. Liu, S.C.; Chen, Y.I.; Tsai, H.Y.; Lin, K.C.; Chen, Y.H. Thermal stability of Ir–Re coatings annealed in oxygen containing atmospheres. *Surf. Coat. Technol.* **2013**, *237*, 105–111. [[CrossRef](#)]
10. Liu, S.C.; Chen, Y.I.; Shyu, J.J.; Tsai, H.Y.; Lin, K.Y.; Chen, Y.H.; Lin, K.C. The chemical inertness of Ir–Re and Ta–Ru coatings in molding B₂O₃–ZnO–La₂O₃-based glass. *Surf. Coat. Technol.* **2014**, *259*, 352–357. [[CrossRef](#)]
11. Zhu, X.Y.; Wei, J.J.; Chen, L.X.; Liu, J.L.; Hei, L.F.; Li, C.M.; Zhang, Y. Anti-sticking Re–Ir coating for glass molding process. *Thin Solid Films* **2015**, *584*, 305–309. [[CrossRef](#)]
12. Uno, K.; Fujino, T.; Nakamori, H. Process for producing mold used for obtaining press molded glass article. U.S. Patent 5,008,002A, 16 April 1991.
13. Hirota, S.; Oogami, Y.; Hashimoto, K. Method of molding a glass composition into an optical element. U.S. Patent 6,776,007B2, 17 August 2004.

14. Kleer, G.; Doell, W. Ceramic multilayer coatings for glass moulding applications. *Surf. Coat. Technol.* **1997**, *94–95*, 647–651. [[CrossRef](#)]
15. Hock, M.; Schäffer, E.; Döll, W.; Kleer, G. Composite coating materials for the moulding of diffractive and refractive optical components of inorganic glasses. *Surf. Coat. Technol.* **2003**, *163–164*, 689–694. [[CrossRef](#)]
16. Lin, C.H.; Duh, J.G.; Yau, B.S. Processing of chromium tungsten nitride hard coatings for glass molding. *Surf. Coat. Technol.* **2006**, *201*, 1316–1322. [[CrossRef](#)]
17. Fischbach, K.D.; Georgiadis, K.; Wang, F.; Dambon, O.; Klocke, F.; Chen, Y.; Yi, A.Y. Investigation of the effects of process parameters on the glass-to-mold sticking force during precision glass molding. *Surf. Coat. Technol.* **2010**, *205*, 312–319. [[CrossRef](#)]
18. Lin, T.N.; Han, S.; Weng, K.W.; Lee, C.T. Investigation on the structural and mechanical properties of anti-sticking sputtered tungsten chromium nitride films. *Thin Solid Films* **2013**, *529*, 333–337. [[CrossRef](#)]
19. Chang, Y.Y.; Cheng, C.M.; Liou, Y.Y.; Tillmann, W.; Hoffmann, F.; Sprute, T. High temperature wettability of multicomponent CrAlSiN and TiAlSiN coatings by molten glass. *Surf. Coat. Technol.* **2013**, *231*, 24–28. [[CrossRef](#)]
20. Chen, Y.I.; Wang, H.H. Oxidation resistance and mechanical properties of Cr–Ta–Si–N coatings in glass molding processes. *Surf. Coat. Technol.* **2014**, *260*, 118–125. [[CrossRef](#)]
21. Chen, Y.I.; Cheng, Y.R.; Chang, L.C.; Lu, T.S. Chemical inertness of Ta–Si–N coatings in glass molding. *Thin Solid Films* **2015**, *584*, 66–71. [[CrossRef](#)]
22. Chen, Y.I.; Cheng, Y.R.; Chang, L.C.; Lee, J.W. Chemical inertness of Cr–W–N coatings in glass molding. *Thin Solid Films* **2015**, *593*, 102–109. [[CrossRef](#)]
23. Chang, L.C.; Zheng, Y.Z.; Gao, Y.X.; Chen, Y.I. Mechanical properties and oxidation resistance of sputtered Cr–W–N coatings. *Surf. Coat. Technol.* **2017**, *320*, 196–200. [[CrossRef](#)]
24. Vepřek, S.; Haussmann, M.; Reiprich, S.; Shizhi, L.; Dian, J. Novel thermodynamically stable and oxidation resistant superhard coating materials. *Surf. Coat. Technol.* **1996**, *86–87*, 394–401. [[CrossRef](#)]
25. Choi, J.B.; Cho, K.; Lee, M.H.; Kim, K.H. Effects of Si content and free Si on oxidation behavior of Ti–Si–N coating layers. *Thin Solid Films* **2014**, *447–448*, 365–370. [[CrossRef](#)]
26. Steyer, P.; Pilloud, D.; Pierson, J.F.; Millet, J.-P.; Charnay, M.; Stauder, B.; Jacquot, P. Oxidation resistance improvement of arc-evaporated TiN hard coatings by silicon addition. *Surf. Coat. Technol.* **2006**, *201*, 4158–4162. [[CrossRef](#)]
27. Nose, M.; Zhou, M.; Nagae, T.; Mae, T.; Yokota, M.; Saji, S. Properties of Zr–Si–N coatings prepared by RF reactive sputtering. *Surf. Coat. Technol.* **2000**, *132*, 163–168. [[CrossRef](#)]
28. Pilloud, D.; Pierson, J.F.; Marco de Lucas, M.C.; Alnot, M. Stabilisation of tetragonal zirconia in oxidized Zr–Si–N nanocomposite coatings. *Appl. Surf. Sci.* **2004**, *229*, 132–139. [[CrossRef](#)]
29. Zeman, P.; Musil, J. Difference in high-temperature oxidation resistance of amorphous Zr–Si–N and W–Si–N films with a high Si content. *Appl. Surf. Sci.* **2006**, *252*, 8319–8325. [[CrossRef](#)]
30. Musil, J. Hard nanocomposite coatings: Thermal stability, oxidation resistance and toughness. *Surf. Coat. Technol.* **2012**, *207*, 50–65. [[CrossRef](#)]
31. Chen, Y.I.; Chang, S.C.; Chang, L.C. Oxidation resistance and mechanical properties of Zr–Si–N coatings with cyclic gradient concentration. *Surf. Coat. Technol.* **2017**, *320*, 168–173. [[CrossRef](#)]
32. Chen, Y.I.; Lin, K.Y.; Wang, H.H.; Cheng, Y.R. Characterization of Ta–Si–N coatings prepared using direct current magnetron co-sputtering. *Appl. Surf. Sci.* **2014**, *305*, 805–816. [[CrossRef](#)]
33. Chen, Y.I.; Lin, K.Y.; Wang, H.H.; Lin, K.C. Thermal stability of TaN, CrTa₂N, TaSiN, and CrTaSiN hard coatings in oxygen-containing atmospheres. *Surf. Coat. Technol.* **2014**, *259*, 159–166. [[CrossRef](#)]
34. Moulder, J.F.; Stickle, W.F.; Sobol, P.E.; Bomben, K.D. *Handbook of X-ray Photoelectron Spectroscopy*; Chastain, J., King, R.C., Eds.; Physical Electronics: Chanhassen, MN, USA, 1995.
35. Oliver, W.C.; Pharr, G.M. An improved technique for determining hardness and elastic modulus using load and displacement sensing indentation experiments. *J. Mater. Res.* **1992**, *7*, 1564–1583. [[CrossRef](#)]
36. Bennett, J.M. *Rough Surfaces*, 2nd ed.; Imperial College Press: London, UK, 1999.
37. Janssen, G.C.A.M.; Abdalla, M.M.; van Keulen, F.; Pujada, B.R.; van Venrooy, B. Celebrating the 100th anniversary of the Stoney equation for film stress: Developments from polycrystalline steel strips to single crystal silicon wafers. *Thin Solid Films* **2009**, *517*, 1858–1867. [[CrossRef](#)]
38. Brantly, W.A. Calculated elastic constants for stress problems associated with semiconductor devices. *J. Appl. Phys.* **1973**, *44*, 534–535. [[CrossRef](#)]

39. Bertóti, I. Characterization of nitride coatings by XPS. *Surf. Coat. Technol.* **2002**, *151–152*, 194–203.
40. Chen, Y.H.; Guruz, M.; Chung, Y.W.; Keer, L.M. Thermal stability of hard TiN/SiN_x multilayer coatings with an equiaxed microstructure. *Surf. Coat. Technol.* **2002**, *154*, 162–166. [[CrossRef](#)]
41. Dong, Y.; Zhao, W.; Yue, J.; Li, G. Crystallization of Si₃N₄ layers and its influences on the microstructure and mechanical properties of ZrN/Si₃N₄ nanomultilayers. *Appl. Phys. Lett.* **2006**, *89*, 121916. [[CrossRef](#)]
42. Abadias, G.; Uglov, V.V.; Saladukhin, I.A.; Zlotski, S.V.; Tolmachova, G.; Dub, S.N.; Janse van Vuuren, A. Growth, structural and mechanical properties of magnetron-sputtered ZrN/SiN_x nanolaminated coatings, *Surf. Coat. Technol.* **2016**, *308*, 158–167. [[CrossRef](#)]



© 2018 by the authors. Licensee MDPI, Basel, Switzerland. This article is an open access article distributed under the terms and conditions of the Creative Commons Attribution (CC BY) license (<http://creativecommons.org/licenses/by/4.0/>).